



Title	SrFe1-xSnxO3-delta nanoparticles with enhanced redox properties for catalytic combustion of benzene
Author(s)	Hashimoto, Kazutaka; Otomo, Ryoichi; Kamiya, Yuichi
Citation	Catalysis Science and Technology, 10(18), 6342-6349 https://doi.org/10.1039/d0cy01154a
Issue Date	2020-09-21
Doc URL	http://hdl.handle.net/2115/82687
Type	article (author version)
Additional Information	There are other files related to this item in HUSCAP. Check the above URL.
File Information	200710_SrFeSnO3_Text-Otomo.pdf



[Instructions for use](#)

1
2
3 $\text{SrFe}_{1-x}\text{Sn}_x\text{O}_{3-\delta}$ nanoparticles with enhanced redox properties for
4 catalytic combustion of benzene
5
6

7 Kazutaka Hashimoto,^a Ryoichi Otomo,^{b,*} and Yuichi Kamiya^b
8

9 ^a Graduate School of Environmental Science and ^b Faculty of Environmental Earth Science,
10 Hokkaido University, Kita 10 Nishi 5, Sapporo 060-0810, Japan.
11

12 Corresponding author:

13 Dr. Ryoichi Otomo

14 E-mail: otomo@ees.hokudai.ac.jp
15

Abstract

A series of Sn-substituted strontium ferrate $\text{SrFe}_{1-x}\text{Sn}_x\text{O}_{3-\delta}$ ($x = 0, 0.25, 0.50, 0.75$ and 1.0) were prepared by the polymerized complex method. Influence of the substitution of Fe in $\text{SrFeO}_{3-\delta}$ with Sn on structural, redox, and catalytic properties was investigated. X-ray diffraction and ^{57}Fe Mössbauer analyses revealed that the partial substitution of Fe with Sn expanded the lattice of the perovskite-type structure, leading to elongation of Fe-O bonds. The partial substitution resulted in the decline of the particle size and the increase of specific surface area. H_2 -TPR and TG measurements in H_2 or O_2 flow indicated that the partial substitution significantly accelerated the redox rates of Fe at $500\text{ }^\circ\text{C}$. Due to the increased surface area and enhanced redox properties, the partially substituted $\text{SrFe}_{1-x}\text{Sn}_x\text{O}_{3-\delta}$ showed higher catalytic activity than $\text{SrFeO}_{3-\delta}$ for combustion of benzene.

1. Introduction

Volatile organic compounds (VOCs) are one of the causes for suspended particulate matter and photochemical oxidants. Hence, the emission of VOCs into the atmosphere is restricted by law in each country.¹⁻³ Various substances are included in VOCs, and a huge amount of VOCs is still used in the painting and cleaning processes.

Combustion is an effective way to decompose and remove VOCs.⁴ For removing aromatic compounds such as benzene, which is low reactive for combustion, catalytic flameless combustion is highly effective. So far various catalysts such as supported metals and transition metal oxides have been developed for the catalytic flameless combustion of VOCs.^{1,2,5}

The perovskite-type metal oxide ABO_3 has excellent catalytic performance against various types of oxidation reactions. It is reported that the combinations of alkaline earth elements or rare earth elements at the A site and transition metals at the B site show high activity for the combustion of VOCs.⁶⁻⁹ Seiyama et al. studied methane complete oxidation using various perovskite-type metal oxides, and found that $LaCoO_3$ and $LaFeO_3$ showed excellent catalytic performance.¹⁰ It was also reported that by partially substituting La with Sr, the transition metals (Co or Fe) at the B site took on unusual high valence of tetravalent

1 for the charge compensation and that these partially substituted materials showed the high
2 oxidation activity, comparable to that of the supported metal catalysts. This is due to the high
3 reactivity of lattice oxygen associated with the reduction of such tetravalent metals to
4 trivalent ones.¹¹

5 SrFeO_3 belongs to the cubic perovskite-type oxide, with Sr^{2+} and Fe^{4+} at the A and
6 B sites, respectively (Fig. 1). SrFeO_3 spontaneously releases lattice oxygen by the reduction
7 of Fe^{4+} to Fe^{3+} under reducing atmosphere or low oxygen partial pressure conditions at high
8 temperature and transforms into brownmillerite-type $\text{SrFeO}_{2.5}$, which is reoxidized to
9 SrFeO_3 under oxidative conditions.

10 Taking advantage of this redox property, SrFeO_3 has been applied to various
11 oxidation reactions as an oxidation catalyst free of precious metals or rare earth elements.^{12–}
12 ²¹ The three-dimensionally ordered macroporous SrFeO_3 had the enhanced redox ability and
13 showed high catalytic activity for toluene combustion compared to the bulk form.²⁰ SrFeO_3
14 in which Sr at the A site was partially substituted with different elements also had enhanced
15 redox ability and exhibited high activity for toluene combustion.^{22,23} The substitution at the
16 B site was effective for tuning the redox properties of SrFeO_3 as well; Hosokawa et al.
17 reported that the partial substitution of Fe at the B site with Ti increased the reoxidation rate.²⁴

1 In addition, it was reported by Wang et al. that the partial substitution of Fe with Sn in BaFeO_3
2 improved the catalytic performance for decomposition of N_2O .²⁵

3 As briefly described above, it is known that the oxidation catalytic activity increases
4 when the redox ability of SrFeO_3 is enhanced. However, to our knowledge, there is only
5 limited number of literature that reports oxidation catalytic properties of SrFeO_3 in which Fe
6 at the B site is partially substituted.²⁶ Furthermore, in order to understand and improve the
7 oxidation catalytic properties of SrFeO_3 , it is indispensable to investigate quantitatively the
8 relationship between substitution of Fe with foreign elements and redox and catalytic
9 properties.

10 In this study, $\text{SrFe}_{1-x}\text{Sn}_x\text{O}_{3-\delta}$ in which Fe was partially or completely substituted
11 with Sn were prepared and the effect of the substitution on the redox ability and catalytic
12 properties for benzene combustion was investigated.

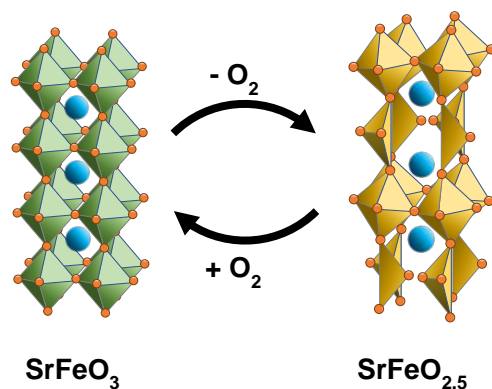


Fig. 1 Interconversion between SrFeO_3 and $\text{SrFeO}_{2.5}$ with release or uptake of oxygen.

2. Experimental

2.1 Materials.

Strontium carbonate, tin(II) chloride dihydrate, ethylene glycol, citric acid monohydrate, benzene, and starch were purchased from FUJIFILM Wako Pure Chemical. Iron acetylacetonate was purchased from Sigma-Aldrich. All the materials were used as received without further purification.

2.2 Preparation of $\text{SrFe}_{1-x}\text{Sn}_x\text{O}_{3-\delta}$.

Perovskite-type oxide samples with nominal compositions of $\text{SrFe}_{1-x}\text{Sn}_x\text{O}_3$ ($x = 0, 0.25, 0.50, 0.75$, and 1.0) were prepared by the polymerized complex method, referring to the procedures reported by Swatsitang et al.²⁷ Strontium carbonate, iron acetylacetonate, tin

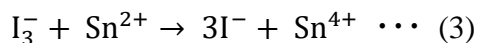
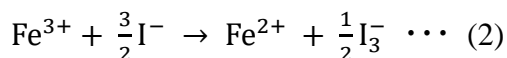
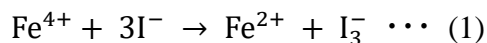
chloride and citric acid were dissolved in ethylene glycol to obtain solution with a molar composition of 1 SrCO_3 : $1-x$ $\text{Fe}(\text{acac})_3$: x SnCl_2 : 24 citric acid: 35 ethylene glycol. After stirred at ambient temperature for 1 h, the solution was heated in an oil bath at 70 °C for 1 h. Then, the temperature was raised to 150 °C and the solution was evaporated to dryness to obtain black solid. The obtained solid was calcined in air in a two-step manner using a muffle furnace. In the first step, the obtained solid was calcined at 300 °C for 5 h. Then, the solid was ground and calcined in air at 1000 °C for 5 h. SrFeO_3 and SrSnO_3 are designated as SFO and SSO, respectively. $\text{SrFe}_{1-x}\text{Sn}_x\text{O}_{3-\delta}$ samples are designated as SFSO_y, where $y = 100x$ (ex; SFSO25 for $x = 0.25$).

2.3 Characterization.

X-ray diffraction (XRD) patterns were measured in 2θ range of 20° – 80° using a Rigaku MiniFlex X-ray diffractometer with Cu K α radiation. Adsorption-desorption isotherms were measured at -196 °C with a MicrotracBEL BELsorp mini analyzer. A powder sample in a glass tube was pretreated in N₂ flow (50 mL/min) at 200 °C for 1 h. Specific surface area of the samples was calculated by the BET method. X-ray photoelectron spectra (XPS) were measured using a JEOL JPC-9010MC spectrometer with Mg K α radiation. A

powder sample was pelletized to a disk, which was pretreated overnight under vacuum. C 1s peak (284.7 eV) was used for the charge correction.

In order to estimate the valence of iron, redox titration of iron was conducted with potassium iodide and tin chloride.²⁸ A powder sample (0.020 g) was dissolved in 1 M hydrochloric acid (10 mL) and the resulting solution was purged with Ar for 10 min. Then, 10 mL of 0.7 M potassium iodide solution was added and stirred at ambient temperature to reduce Fe⁴⁺ and Fe³⁺ following the equations 1 and 2. The amount of the formed I₃⁻ was determined by a titration with SnCl₂/HCl solution following the equation 3. The average valence of iron was estimated from the amount of the formed I₃⁻.



⁵⁷Fe Mössbauer spectra were obtained using a Laboratory equipment corporation VT-6000 spectrometer with a ⁵⁷Co γ-ray source. To keep the amount of iron in specimen constant, the amount of sample was varied. The desired amount of a sample was diluted with starch and pelletized to a specimen wafer. The obtained spectra were deconvoluted and fitted

1 with Lorentzian curves by using a Mosswin program.

2 Temperature-programmed reduction of samples with H₂ (H₂-TPR) was conducted
3 using a MicrotracBEL BEL-CAT analyzer. The amount of a sample was varied to keep the
4 amount of iron in specimen constant. The powder sample in a quartz tube was pretreated in
5 O₂ flow (29 mL/min) at 700 °C for 1 h. After cooled to 100 °C, the sample was purged by
6 He flow (29 mL/min) for 0.5 h. Then, a TPR profile was obtained by heating the sample in
7 5% H₂/Ar flow (29 mL/min) from 100 to 700 °C at a heating rate of 10 °C/min and the
8 concentration of H₂ was monitored by a thermal conductivity detector.

9 To investigate redox properties of samples at high temperature, weight change of
10 the samples due to release or uptake of oxygen was measured at 500 °C on a Rigaku TG8120
11 thermogravimetric analyzer. A powder sample (20 mg) was pretreated in pure O₂ at a flow
12 rate of 50 mL/min at 700 °C for 1 h and then the sample was cooled to 500 °C in 5 % O₂/He
13 (100 mL/min). After the weight became constant, the gas flow was switched to 5 % H₂/He
14 (100 mL/min) and the weight loss due to the reduction was monitored. After the weight
15 became almost constant, the gas flow was switched back to 5 % O₂/He (100 mL/min) and
16 the weight gain due to the oxidation was monitored.

2.4 Evaluation of catalytic activity for combustion of benzene.

Catalytic combustion of benzene was operated in a fixed bed flow reactor at atmospheric pressure. The powdery catalyst (0.10 g) was loaded in a quartz tube (i.d. = 8 mm) and pretreated in pure O₂ flow (15 mL/min) at 700 °C for 1 h. After cooled to 100 °C in the O₂ flow, the gas flow was switched to the reactant feed (50 mL/min) with molar composition of 1 C₆H₆/ 20 O₂/ 79 He, where weight hourly space velocity was 30,000 mL/g·h. Then the reactor was heated from 100 to 700 °C at a heating rate of 10 °C/min. The effluent gas was analyzed by an on-line gas chromatograph (Shimadzu GC8A) with a flame ionization detector.

3. Results and discussion

3.1 Structure of SrFe_{1-x}Sn_xO_{3-δ}.

XRD patterns of SrFe_{1-x}Sn_xO_{3-δ} samples are shown in Fig. 2. SFO and SSO showed diffraction patterns assigned to tetragonal SrFeO_{2.86} (JCPDS #39-954) and cubic SrSnO₃ (JCPDS # 22-1142), respectively. For SFSO samples, the diffraction line of SFO shifted to lower angles as the Sn content increased. Since the ionic radius of Sn⁴⁺ (0.690 Å) is much smaller than that of Sr²⁺ (1.44 Å) at the A site, Sn⁴⁺ is not able to occupy the A site.

1 Presumably, Sn^{4+} occupied the B site, as the ionic radius of Sn^{4+} and Fe^{4+} with octahedral
2 coordination (0.585 Å) are similar.²⁹ Therefore, it is considered that the substitution of Fe^{4+}
3 at the B site with Sn^{4+} , which has a large ionic radius, expanded the lattice and caused the
4 low-angle shift of the diffraction lines (Table S1). For SFSO samples, no diffraction line of
5 SFO nor SSO was observed, indicating that SFSO samples were not mixtures of SFO and
6 SSO, but solid solutions containing both Fe and Sn at the B site.

7 Compared with SFO and SSO, diffraction lines of SFSO samples were broad. The
8 crystallite size for each sample was calculated by using the Scherrer's equation on the
9 diffraction lines of $2\theta = 31 - 33^\circ$ (Table 1). For both SFO and SSO, the crystallite size was
10 43.6 nm, while the size was 25.5 nm for SFSO75. The decrease in the crystallite size resulted
11 in the broadening of diffraction lines for SFSO samples. In addition, the distortion of the
12 crystallite caused by random arrangement of Fe and Sn might bring the broadening of
13 diffraction lines.

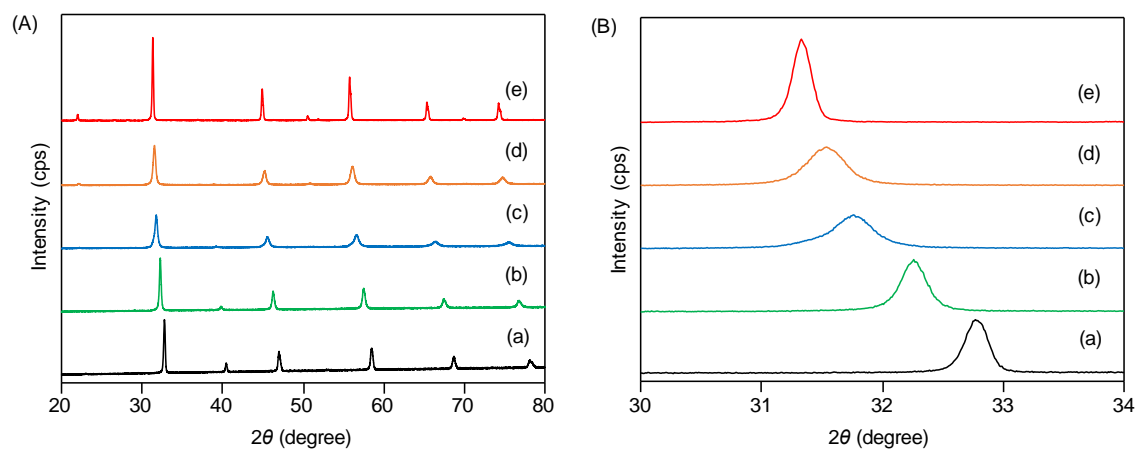


Fig. 2 XRD patterns of $\text{SrFe}_{1-x}\text{Sn}_x\text{O}_{3-\delta}$ in 2θ range of (A) 20° – 80° , and (B) 30° – 34° . (a) SFO, (b) SFSO25, (c) SFSO50, (d) SFSO75, and (e) SSO.

Table 1 Crystallite size and surface area for $\text{SrFe}_{1-x}\text{Sn}_x\text{O}_{3-\delta}$.

Sample	Crystallite size ^a (nm)	Surface area ^b (m ² /g)
SFO	42.6	0.4
SFSO25	37.2	1.9
SFSO50	24.2	8.1
SFSO75	25.5	11.7
SSO	42.6	0.3

^a Calculated by Scherrer's equation, ^b BET surface area calculated from a N₂ adsorption isotherm.

Fig. 3 shows SEM images of SFO, SFSO50, and SSO. SFO had particles without specific morphology larger than 1 μm and SSO had round particles of sub-micrometers. For both samples, the particle sizes were much larger than the crystallite sizes determined by the Scherrer's equation (Table 1), suggesting that the primary particles highly aggregated to form the secondary ones. SFSO50 had fine particles of 50 nm or less, which was close to the size of crystallite. Similarly, fine particles were observed in SFSO25 and SFSO75 (not shown). The incorporation of Sn favorably suppressed the aggregation of the primary particles, resulting in the highly dispersed fine particles, as similar behavior was reported in the early literature.^{30,31}

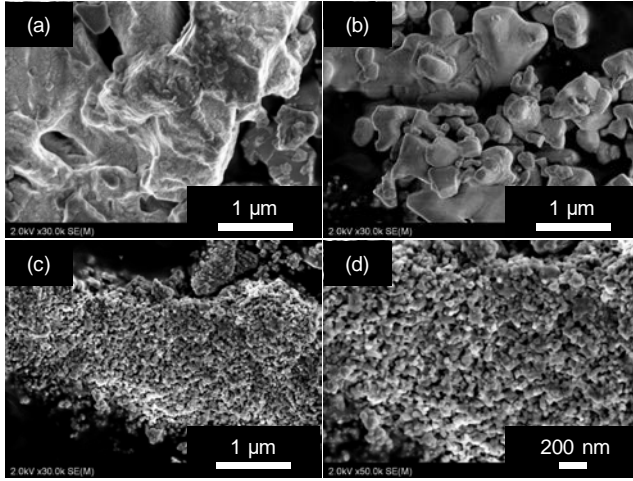


Fig. 3 SEM images of $\text{SrFe}_{1-x}\text{Sn}_x\text{O}_{3-\delta}$. (a) SFO, (b) SSO, and (c, d) SFSO50.

By nitrogen adsorption-desorption measurements (Table 2), the specific surface area of SFO was determined to be $0.4 \text{ m}^2/\text{g}$. The specific surface area was increased by the partial substitution with Sn and reached a maximum of $11.7 \text{ m}^2/\text{g}$ for SFSO75. However, the specific surface area of SSO was conversely the smallest of the samples. Due to the highly dispersed fine particles, as observed by SEM, SFSO samples had the large specific surface area.

^{57}Fe Mössbauer spectroscopy was performed to investigate the chemical state of Fe in the samples (Fig. 4). The center of each spectrum with respect to the reference (Fe_2O_3) is called isomer shift (IS), which reflects the d -electron density and shifts to positive as the electron density increases. The split width of each spectrum is called the quadrupole splitting (QS), which reflects the magnitude of the electric field gradient around the Fe nucleus.

Symmetry of coordination environment affects QS; in a highly symmetric coordination environment, QS is close to zero.³²

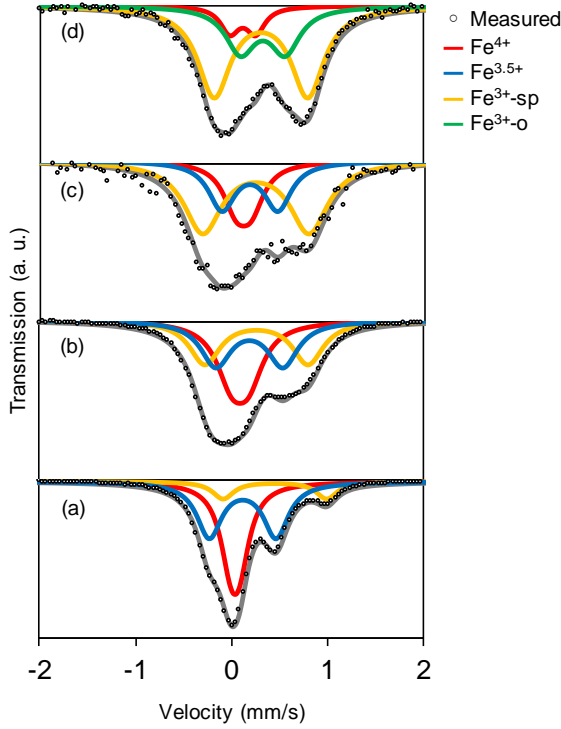


Fig. 4 ^{57}Fe Mössbauer spectra of $\text{SrFe}_{1-x}\text{Sn}_x\text{O}_{3-\delta}$. (a) SFO, (b) SFSO25, (c) SFSO50, and (d) SFSO75.

The obtained spectra were deconvoluted into three spectra (Table 2). Spectra with small QS values were attributed to highly symmetric octahedral Fe^{4+} .^{33–35} The spectra with QS values of ~ 1 were Fe^{3+} with asymmetric square pyramidal coordination ($\text{Fe}^{3+}\text{-sp}$).^{33–35}

1 The spectra with intermediate QS values were $\text{Fe}^{3.5+}$, which was observed with an
2 intermediate electronic state between Fe^{4+} and Fe^{3+} because electron transfer with oxygen
3 constantly occurs during the measurement.³³⁻³⁶ The proportion of Fe^{4+} and Fe^{3+} in each
4 sample was calculated from the area of these spectra, where $\text{Fe}^{3.5+}$ was equally allocated to
5 Fe^{3+} and Fe^{4+} . The proportion of Fe^{4+} was 66% in SFO but decreased with the increase in the
6 Sn content and became 24% in SFSO75.

7 SFSO samples showed higher QS values of Fe^{4+} than SFO, suggesting that the
8 originally symmetric octahedral coordination was distorted by the incorporation of Sn at the
9 B sites. It is consistent with the distortion of crystallite observed by XRD. For SFSO samples,
10 the positive shift of IS values of Fe^{4+} and $\text{Fe}^{3.5+}$ indicated that the *d*-electron density of Fe^{4+}
11 was increased by the substitution with Sn. It is likely that the *d*-electron density of Fe was
12 increased due to the elongation of Fe-O bond accompanied with the expansion of the lattice.
13 For SFSO75, the IS value of $\text{Fe}^{3.5+}$ was increased significantly. It might not be attributed to
14 $\text{Fe}^{3.5+}$, but to Fe^{3+} in octahedral coordination.³⁴ These results indicated that the substitution
15 with Sn caused the elongation of Fe-O bonds and the distortion of coordination environment
16 around Fe.

Table 2 Mössbauer parameters and Fe valences of $\text{SrFe}_{1-x}\text{Sn}_x\text{O}_{3-\delta}$.

Sample	IS ^a (mm/s)			QS ^b (mm/s)			Area (%)			Fe ³⁺ /Fe ⁴⁺ ^c (%)
	Fe ³⁺	Fe ^{3.5+}	Fe ⁴⁺	Fe ³⁺	Fe ^{3.5+}	Fe ⁴⁺	Fe ³⁺	Fe ^{3.5+}	Fe ⁴⁺	
SFO	0.45	0.12	0.04	1.08	0.69	0.09	11.9	44.8	43.3	34/ 66
SFSO25	0.26	0.19	0.09	1.07	0.70	0.18	31.6	31.7	36.7	48/ 52
SFSO50	0.24	0.18	0.11	1.10	0.58	0.16	53.5	25.8	20.7	66/ 34
SFSO75	0.30	0.32 ^d	0.11	0.97	0.46	0.27	61.6	28.4	10.0	76/ 24

^a Isomer shift, ^b Quadrupole splitting, ^c Abundance of Fe species, ^d Fe³⁺ in octahedral coordination.

Surface species on the samples were examined by XPS (Fig. S1). Fe 2p_{1/2} spectra of SFO and SFSO samples showed broad peaks at ~723 eV, which were attributed to Fe³⁺.³⁷ Sn 3d spectra confirmed that Sn took tetravalent (Sn⁴⁺) in these samples.³⁸ The presence of multiple component was observed in O 1s spectra; the peaks at 528, 531, and 533 eV were assigned to lattice oxygen, carbonate oxygen, and adsorbed species such as H₂O, respectively.³⁷

Table 3 shows surface compositions estimated by XPS. The surface of SFO was rich in Sr, followed by O and Fe. For SFSO samples, Fe was largely decreased, and Sn appeared instead. Despite the low surface density of Fe, the amount of the surface Fe per unit sample

mass for SFSO samples was a little larger than that for SFO due to the large specific surface area.

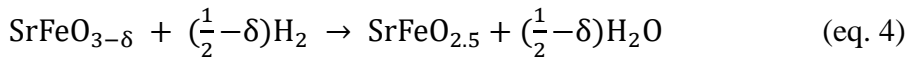
Table 3 Surface compositions of $\text{SrFe}_{1-x}\text{Sn}_x\text{O}_{3-\delta}$ samples.

Sample	Composition ^a				Density of Fe ^b (/nm ²)	Amount of surface Fe (μmol/g)
	Sr	Fe	Sn	O		
SFO	0.53	0.17	0.00	0.30	0.90	0.59
SFSO25	0.39	0.06	0.10	0.45	0.34	1.05
SFSO50	0.50	0.03	0.12	0.35	0.15	2.05
SFSO75	0.32	0.01	0.22	0.45	0.06	1.13
SSO	0.36	0.00	0.23	0.41	0.00	0.00

^a Surface composition determined by XPS, ^b Density on (111) facet of tetragonal $\text{SrFeO}_{3-\delta}$.

3.2 Redox properties of $\text{SrFe}_{1-x}\text{Sn}_x\text{O}_{3-\delta}$.

H_2 -TPR profiles were measured to evaluate the reduction properties of each sample (Fig. 5). SFO showed a large reduction peak at 450 °C, which was attributed to the reduction of Fe^{4+} to Fe^{3+} with multiple structural changes, described in the equation 4.^{14,35}



In fact, the sample after the H_2 -TPR measurement showed an XRD pattern assignable to brownmillerite-type $\text{SrFeO}_{2.5}$ (JCPDS #17-0932) (Fig. S2). A small reduction peak at

1 ~550 °C might be attributed to the reduction of Fe^{3+} to Fe^{2+} .³⁵ The amount of Fe^{4+} calculated
2 from the hydrogen consumption was close to those estimated from Mössbauer spectroscopy
3 and iodometric titration (Table 4). Titration experiments confirmed that no Fe^{4+} remained in
4 SFO after the H_2 -TPR measurement. These results strongly supported that the peak around
5 450 °C was due to the reduction of Fe^{4+} to Fe^{3+} .

6 For SFSO samples, this reduction peak shifted to lower temperature and the peak
7 area decreased as the increase in the Sn content. Probably because the Fe-O bond was
8 weakened by the substitution with Sn, as observed by Mössbauer spectroscopy, Fe^{4+} was
9 easily reduced by H_2 at lower temperature. For SSO, hydrogen consumption was slightly
10 observed at 550 °C or higher. Since there was no change in the bulk structure for SSO after
11 the measurement (Fig. S2), it is speculated that only Sn near the surface was reduced. For
12 SFSO75, in addition to the low-temperature peak (250 – 350 °C) attributed to Fe^{4+} to Fe^{3+} , a
13 slight reduction peak appeared at around 450 °C, probably due to the reduction of a slight
14 amount of Fe^{3+} to Fe^{2+} . It was confirmed that the reduction of Fe^{3+} to Fe^{2+} did not occur when
15 benzene was used as a reducing agent instead of H_2 and that the redox of $\text{Fe}^{3+}/\text{Fe}^{2+}$ did not
16 participate in the oxidation of benzene.

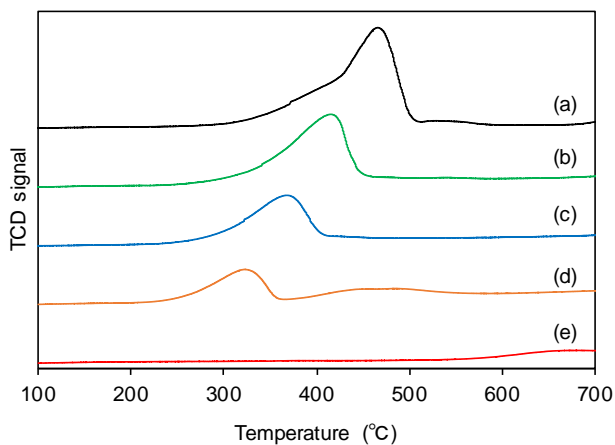


Fig. 5 H₂-TPR profiles of SrFe_{1-x}Sn_xO_{3-δ}. (a) SFO, (b) SFSO25, (c) SFSO50, (d) SFSO75 and (e) SSO.

Table 4 Fe content and proportion of Fe⁴⁺ for SrFe_{1-x}Sn_xO_{3-δ}.

Sample	Fe content (mmol/g)	Fe ⁴⁺ / (Fe ³⁺ + Fe ⁴⁺)		
		Mössbauer	Titration	H ₂ -TPR
SFO	5.22	0.66	0.66	0.75
SFSO25	3.62	0.52	0.56	0.49
SFSO50	2.24	0.34	0.33	0.31
SFSO75	1.05	0.24	0.40	0.20
SSO	0.00	-	-	-

Redox properties of the samples at high temperature were investigated by using a

TG analyzer (Fig. S3). Based on the weight changes, the amount of Fe involved in the redox

was calculated (Fig. 6). For SFO, 3.0 mmol/g of Fe, which corresponded to 58% of the total

1 Fe, took tetravalent under oxidative conditions. As the substitution of Fe with Sn increased,
2 the amount of Fe^{4+} decreased; 1.8, 0.5, and 0.2 mmol/g of Fe for SFSO25, SFSO50, and
3 SFSO75, respectively. For SFO and SFSO samples, Fe^{4+} was almost completely reduced to
4 Fe^{3+} under reductive conditions. SSO did not show any redox properties measured by weight
5 change on TG analysis (not shown).

6 The obtained TG curve was differentiated, and initial redox rates per Fe was
7 calculated (Fig. 6) For SFO, the oxidation/reduction rates were 0.02 and 0.03 s^{-1} , respectively.
8 These rates were increased by the substitution with Sn and both rates reached the maximum
9 (0.17 s^{-1}) for SFSO75. These results indicated that while the amount of Fe^{4+} involved in the
10 redox was decreased, the redox rate per Fe was largely increased by the substitution with Sn.
11 Presumably, for SFSO samples, the elongation of Fe-O bonds with the increased *d*-electron
12 density facilitated the cleavage of Fe-O bonds and caused the increase in the reduction rate.
13 Upon reduction, the perovskite-type structure of SFO transformed to the brownmillerite-type
14 one (Fig. S2). Consequently, the reoxidation entailed the reverse transformation to the
15 perovskite-type structure. On the other hand, for SFSO samples, the perovskite-type structure
16 was maintained even after the reduction (Fig. S2), and therefore the reoxidation proceeded
17 rapidly owing to no such structural interconversion.^{39,40}

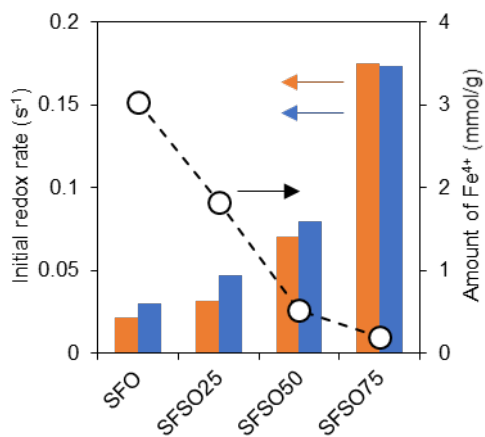


Fig. 6 Initial redox rate and the amount of Fe⁴⁺ under oxidative conditions for SrFe_{1-x}Sn_xO_{3-δ} determined by TG.

3.3 Combustion of benzene over SrFe_{1-x}Sn_xO_{3-δ}.

Catalytic combustion of benzene was performed using SFO, SFSO, and SSO samples (Fig. 7). No product other than CO₂ and H₂O was detected by a thermal conductivity detector and a quadruple mass spectrometer, indicating that benzene was completely oxidized in all cases. When the reaction was performed without a catalyst, the concentration of benzene in the gas phase was hardly decreased, confirming that the reaction did not at all occur in the absence of a catalyst.

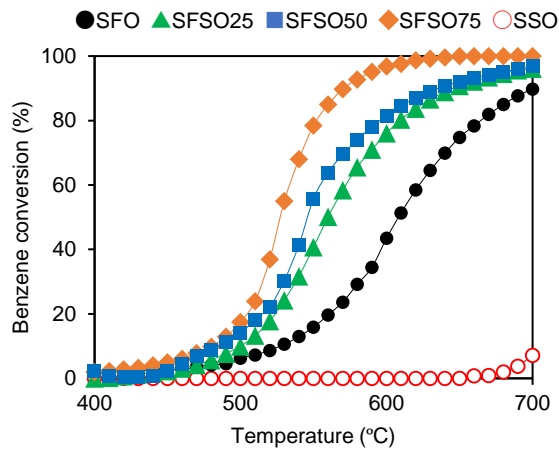


Fig. 7 Light-off curves for catalytic combustion of benzene over $\text{SrFe}_{1-x}\text{Sn}_x\text{O}_{3-\delta}$.

For SFO, the oxidation of benzene started at $\sim 450^\circ\text{C}$ and the conversion reached 50 and 90% at 608 and 700°C , respectively. For SFSO samples, the conversion of benzene increased significantly between 500 and 550°C . Particularly, SFSO75 showed the highest activity, attaining the 50 and 90% conversion at around 530 and 570°C , respectively. At further high temperature, the conversion increased and reached 99% at around 630°C . SSO showed only very low catalytic activity and the conversion was still 7% even at 700°C . Hence, only Fe species was essentially active for the oxidation of benzene.

SFO, SFSO25, and SFSO50 showed the gradual increase of the conversion at $\sim 600^\circ\text{C}$ or higher and did not reach 99% even at 700°C . It is known that $\text{SrFeO}_{3-\delta}$

1 spontaneously releases oxygen at high temperature even oxidative conditions and exists in
2 the reduced form.^{16,35,41–43} For these three samples, the amount of Fe^{4+} was likely to decrease
3 during the reaction at a relatively high temperature and it became difficult to attain high
4 conversion, even though the reaction rate over the remaining Fe^{4+} increased. On the other
5 hand, SFSO75 had high activity and so the overall reaction proceeded at a relatively low
6 temperature, attaining the high conversion of benzene over 99%.

7 Catalytic performance was compared between SFO, SFSO75, and LaFeO_3 , which
8 is an iron-based perovskite-type oxide highly active for various oxidation reactions (Fig.
9 S4).^{44,45} LaFeO_3 showed gradual increase in the conversion of benzene at 500 °C or higher
10 and the light-off curve for LaFeO_3 was between those for SFSO75 and SFO. This result
11 clearly demonstrated the superior catalytic performance of SFSO75 to LaFeO_3 .

12 In order to examine a relationship between benzene adsorption properties and
13 catalytic activity, Benzene-TPD was conducted on SFO, SFSO and SSO samples (Fig. S5).
14 SFSO75 showed the largest desorption amount of benzene (4.7 $\mu\text{mol/g}$) and gave a
15 desorption peak at ~120 °C. SFSO50 also showed a large desorption amount of benzene (2.6
16 $\mu\text{mol/g}$). SFO, SFSO25 and SSO hardly showed the desorption of benzene. Thus, no clear
17 relationship between the benzene adsorption characteristics and the catalytic activity implied

1 that that the benzene adsorption properties did not determine the catalytic performance.

2 As shown in Table 2, SFSO samples had the larger specific surface area than SFO.
3 To investigate the effect of the surface area on the catalytic activity, the reaction was
4 performed by using five times the amount of SFO so that the effective surface area became
5 equal to that of SFSO25 (Fig. S6). Indeed, the high loading of SFO shifted the light-off curve
6 to low temperature. However, SFSO25 still gave higher conversion of benzene at relatively
7 low temperature up to 600 °C. The activity was certainly affected by the specific surface area,
8 but it is supposed that the reason for the high activity of SFSO samples was not only this but
9 also the high activity per Fe.

10 Fig. 8 shows a relationship between the turnover frequency per surface Fe at 500 °C
11 and the initial redox rates of Fe determined by the measurement on TG. As the redox rates
12 increased, the turnover frequency was increased. The correlation suggests that the catalytic
13 activity per Fe was determined by the redox rates. Considering the above results, the whole
14 activity of SFO and SFSO catalysts was governed by the redox rate per Fe as well as the
15 specific surface area. The partial substitution of Fe with Sn favorably enhanced both factors
16 and consequently SFSO samples showed high catalytic activity than SFO.

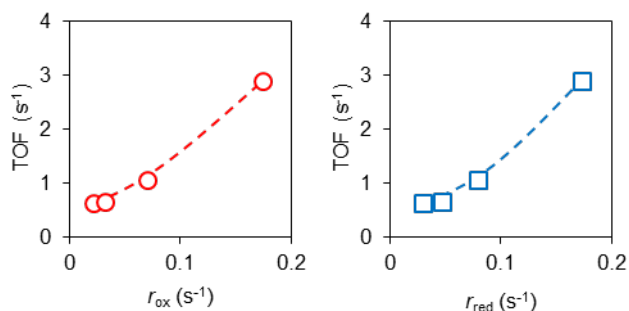


Fig. 8 Relationship between catalytic activity and redox rates. Turnover frequency was calculated as mol of benzene converted at 500 °C per mol of surface Fe⁴⁺.

4. Conclusion

Perovskite-type oxide SFO, SFSO, and SSO samples were prepared by the polymerized complex method. SFSO samples were the solid solutions of SFO and SSO. The incorporation of Sn in the lattice elongated the Fe-O bonds and distorted the coordination environment around Fe. SFSO samples had smaller particle size and larger specific surface area than SFO and SSO. The partial substitution with Sn sacrificed the amount of Fe⁴⁺ under oxidative conditions at high temperature, but largely increased the redox rates of Fe⁴⁺. Due to the large specific surface area and the enhanced redox rates, SFSO samples showed higher catalytic activity than SFO and SSO for the combustion of benzene. Particularly, SFSO75, which had the largest surface area and the highest redox rates, showed the best catalytic

1 performance.

2

3 **Supporting Information**

4 Additional data on characterization and catalytic reactions is provided as *Supporting*
5 *Information*.

6

7 **Conflicts of interest**

8 There are no conflicts of interest to declare.

9

10 **Acknowledgement**

11 The analysis of XPS was conducted with the instrument at the Institute for Catalysis,
12 Hokkaido University.

13

14

References

- 1 C. He, J. Cheng, X. Zhang, M. Douthwaite, S. Patisson and Z. Hao, *Chem. Rev.*,
2019, **119**, 4471–4568.
- 2 M. S. Kamal, S. A. Razzak and M. M. Hossain, *Atmos. Environ.*, 2016, **140**, 117–
134.
- 3 A. O. Rusu and E. Dumitriu, *Environ. Eng. Manag. J.*, 2003, **2**, 273–302.
- 4 M. Tomatis, H. Xu, J. He and X. Zhang, *J. Chem.*, 2016, **2016**, 1–15.
- 5 S. Morales-Torres, F. Carrasco-Marín, A. F. Pérez Cadenas and F. J. Maldonado-
Hódar, *Catalysts*, 2015, **5**, 774–799.
- 6 H. Einaga, S. Hyodo and Y. Teraoka, *Top. Catal.*, 2010, **53**, 629–634.
- 7 Y. Luo, K. Wang, Q. Chen, Y. Xu, H. Xue and Q. Qian, *J. Hazard. Mater.*, 2015,
2015, **296**, 17–22.
- 8 K. L. Pan, G. T. Pan, S. Chong and M. B. Chang, *J. Environ. Sci.*, 2018, **69**, 205–
216.
- 9 M. Zang, C. Zhao, Y. Wang and S. Chen, *J. Saudi Chem. Soc.*, 2019, **23**, 645–654.
- 10 H. Arai, T. Yamada, K. Eguchi and T. Seiyama, *Appl. Catal.*, 1986, **26**, 265–276.
- 11 T. Seiyama, *Catal. Rev.*, 1992, **34**, 281–300.

- 1 12 S. Shibata, K. Sugahara, K. Kamata and M. Hara, *Chem. Commun.*, 2018, **54**, 6772–
2 6775.
- 3 13 C. Srilakshmi, R. Saraf and C. Shivakumara, *Ind. Eng. Chem. Res.*, 2015, **54**, 7800–
4 7810.
- 5 14 H. Falcón, J. A. Barbero, J. A. Alonso, M. J. Martínez-Lope and J. L. G. Fierro,
6 *Chem. Mater.*, 2002, **14**, 2325–2333.
- 7 15 H. X. Dai, C. F. Ng and C. T. Au, *Catal. Letters*, 1999, **57**, 115–120.
- 8 16 K. Tamai, S. Hosokawa, H. Okamoto, H. Asakura, K. Teramura and T. Tanaka, *ACS*
9 *Appl. Mater. Interfaces*, 2019, **11**, 26985–26993.
- 10 17 X. Wang, X. J. Gao, L. Qin, C. Wang, L. Song, Y. N. Zhou, G. Zhu, W. Cao, S. Lin,
11 L. Zhou, K. Wang, H. Zhang, Z. Jin, P. Wang, X. Gao and H. Wei, *Nat. Commun.*,
12 2019, **10**, 1–8.
- 13 18 M. Y. Leiw, G. H. Guai, X. Wang, M. S. Tse, C. M. Ng and O. K. Tan, *J. Hazard.*
14 *Mater.*, 2013, **260**, 1–8.
- 15 19 K. Tamai, S. Hosokawa, K. Onishi, C. Watanabe, K. Kato, H. Asakura, K. Teramura
16 and T. Tanaka, *ACS Catal.*, 2020, **10**, 2528–2537.
- 17 20 K. Ji, H. Dai, J. Deng, L. Zhang, F. Wang, H. Jiang and C. T. Au, *Appl. Catal. A*

- 1 *Gen.*, 2012, **425–426**, 153–160.
- 2 21 S. Yagi, I. Yamada, H. Tsukasaki, A. Seno, M. Murakami, H. Fujii, H. Chen, N.
- 3 Umezawa, H. Abe, N. Nishiyama and S. Mori, *Nat. Commun.*, 2015, **6**, 1–6.
- 4 22 K. Ji, H. Dai, J. Deng, X. Li, Y. Wang, B. Gao, G. Bai and C. Tong, *Appl. Catal. A*
- 5 *Gen.*, 2012, **447–448**, 41–48.
- 6 23 K. Ji, H. Dai, J. Deng, H. Jiang, L. Zhang, H. Zhang and Y. Cao, *Chem. Eng. J.*,
- 7 2013, **214**, 262–271.
- 8 24 A. Demizu, K. Beppu, S. Hosokawa, K. Kato, H. Asakura, K. Teramura and T.
- 9 Tanaka, *J. Phys. Chem. C*, 2017, **121**, 19358–19364.
- 10 25 C. Huang, Y. Zhu, X. Wang, X. Liu, J. Wang and T. Zhang, *J. Catal.*, 2017, **347**, 9–
- 11 20.
- 12 26 A. A. Yaremchenko, V. V. Kharton, A. A. Valente, S. A. Veniaminov, V. D.
- 13 Belyaev, V. A. Sobyandin and F. M. B. Marques, *Phys. Chem. Chem. Phys.*, 2007,
- 14 **9**, 2744–2752.
- 15 27 S. Hunpratub, A. Karaphun, S. Phokha and E. Swatsitang, *Appl. Surf. Sci.*, 2016,
- 16 **380**, 52–59.
- 17 28 A. S. Urusova, V. A. Cherepanov, T. V. Aksenova, L. Y. Gavrilova and E. A.

- 1 Kiselev, *J. Solid State Chem.*, 2013, **202**, 207–214.
- 2 29 R. D. Shannon, *Acta Cryst.*, 1976, **A32**, 751–767.
- 3 30 M. Amsif, D. Marrero-Lopez, J. C. Ruiz-Morales, S. N. Savvin, M. Gabás and P.
- 4 Nunez, *J. Power Sources*, 2011, **196**, 3461–3469.
- 5 31 A. J. Fernández-Ropero, J. M. Porras-Vázquez, A. Cabeza, P. R. Slater, D. Marrero-
- 6 López and E. R. Losilla, *J. Power Sources*, 2014, **249**, 405–413.
- 7 32 P. Gütllich and V. Schünemann, *Spectrosc. Eur.*, 2014, **24**, 21–32.
- 8 33 P. Adler, A. Lebon, V. Damljanić, C. Ulrich, C. Bernhard, A. V. Boris, A. Maljuk,
- 9 C. T. Lin and B. Keimer, *Phys. Rev. B*, 2006, **73**, 094451.
- 10 34 P. S. Beurmann, V. Thangadurai and W. Weppner, *J. Solid State Chem.*, 2003, **174**,
- 11 392–402.
- 12 35 H. Ikeda, S. Nikata, E. Hirakawa, A. Tsuchida and N. Miura, *Chem. Eng. Sci.*, 2016,
- 13 **147**, 166–172.
- 14 36 J. P. Hodges, S. Short, J. D. Jorgensen, X. Xiong, B. Dabrowski, S. M. Mini and C.
- 15 W. Kimball, *J. Solid State Chem.*, 2000, **151**, 190–209.
- 16 37 M. Ghaffari, H. Huang, O. K. Tan and M. Shannon, *CrystEngComm*, 2012, **14**,
- 17 7487–7492.

- 1 38 A. A. Kumar, A. Kumar, J. K. Quamara, G. R. Dillip, S. W. Joo and J. Kumar, *RSC*
2 *Adv.*, 2015, **5**, 17202–17209.
- 3 39 C. Haavik, T. Atake and S. Stølen, *Phys. Chem. Chem. Phys.*, 2002, **4**, 1082–1087.
- 4 40 E. Bakken, S. Stølen, T. Norby, R. Glenne and M. Budd, 2004, **167**, 367–377.
- 5 41 B. C. Tofield, C. Greaves and B. E. F. Fender, *Mater. Res. Bull.*, 1975, **10**, 737–746.
- 6 42 Y. Takeda, K. Kanno, T. Takada, O. Yamamoto, M. Takano, N. Nakayama and Y.
7 Bando, *J. Solid State Chem.*, 1986, **63**, 237–249.
- 8 43 J. Dou, E. Krzystowczyk, X. Wang, T. Robbins, L. Ma, X. Liu and F. Li,
9 *ChemSusChem*, 2020, **13**, 385–393.
- 10 44 H. Zhu, P. Zhang and S. Dai, *ACS Catal.*, 2015, **5**, 6370–6385.
- 11 45 S. Royer, D. Duprez, F. Can, X. Courtois, C. Batiot-Dupeyrat, S. Laassiri and H.
12 Alamdari, *Chem. Rev.*, 2014, **114**, 10292–10368.

13